ADVANCED MATERIALS INTERFACES
Open Access
www.advmatinterfaces.de

Check for updates

Borophene-Based Ultrasensitive and Broadband Photodetectors

Yaser Abdi, Alireza Eskandari, Zahra Alavi, Anousha Khamsavi, Mahsa Etminan, Mobina Zahedi, Masoud Taleb, and Nahid Talebi**

Photodetectors based on vertical junctions between 2D materials and silicon offer enhanced sensitivity, reduced size, and better integrability with other systems. In these detectors, 2D materials are typically grown on metallic crystalline substrates and then transferred onto silicon to form a van der Waals junction between the 2D and silicon. In this work, χ_3-phase borophene is directly grown on single-crystal silicon wafers, resulting in excellent Schottky junctions between borophene and silicon. This approach eliminates impurities often introduced during the transfer process, which is commonly performed using polymethyl methacrylate, ensuring a smooth fabrication process and a reliable electrical junction. Optoelectronic measurements of the borophene-based detector on n-type silicon demonstrate high sensitivity, reaching several amps per watt across a wide wavelength range from ultraviolet to infrared. This sensitivity is approximately ten times higher than that of detectors fabricated by transferring 2D materials onto silicon. Additionally, the response times of the fabricated detector are measured at 35 µs for the rise time and 225 µs for the fall time. These exceptional results are attributed to the superior junction formed through direct borophene growth on silicon, paving the way for advanced photodetectors with enhanced light–matter interaction efficiency in integrated silicon-based circuits and technologies.

1. Introduction

After the successful growth of graphene and post-graphene 2D materials, numerous electronic devices have been fabricated based on these materials.[1–7] In particular, the use of 2D materials can play an important role in enhancing the performance of photodetectors, due to their high mobility and tunable optical properties.[8–10] However, 2D materials have rather low light absorption efficiency due to the small volume of interaction with light, resulting in significantly-reduced sensitivities.[11] Therefore, the idea of combining 2D materials with bulk materials opened up new avenues for researchers. In this type of photodetector, light absorption occurs through both the 2D material and the bulk material, leading to increased absorption efficiency.[12,13] Essentially, the bulk material is primarily responsible for light absorption and the generation of electron–hole pairs, while the 2D material acts as a highly mobile charge carrier transporter. This approach effectively improves the absorption efficiency of photodetectors based solely on 2D materials.

Silicon, as a crucial material in the electronic and optoelectronic device fabrication process, is an ideal choice for the bulk material. Consequently, several reports have highlighted the fabrication of photodetectors based on the electrical junction between silicon and 2D materials.[13,14] In such photodetectors, specific types of 2D materials are selected to create either p–n or Schottky electrical junctions with the silicon substrate. For metallic 2D materials, the Schottky junction is created, and the doping type of silicon and the work function of the semiconducting material play crucial roles in forming an effective Schottky junction. Since the efficient generation of electron–hole pairs occurs in the depletion region of the electrical junction, vertical junctions are considered one of the best types of electrical junctions. In this configuration, the entire detector area corresponds to the depletion region and, consequently, the active area. Light passes through the thin 2D material and enters the depletion region created at the interface, resulting in the production of electron–hole pairs.

In the past, transferring 2D materials on silicon has been used to create vertical connections. Chemical vapor deposition (CVD) is a high-quality and cost-effective method for growing 2D materials.[8,15] Typically, to establish vertical connections between silicon and 2D materials, researchers first grow the 2D

Y. Abdi, A. Eskandari, Z. Alavi, A. Khamsavi, M. Etminan, M. Zahedi
Nanophysics Research Laboratory
Department of Physics
University of Tehran
Tehran 14395–547, Iran
E-mail: y.abdi@ut.ac.ir
Y. Abdi, M. Taleb, N. Talebi
Institute of Experimental and Applied Physics
Kiel University
24118 Kiel, Germany
E-mail: talebi@physik.uni-kiel.de
The ORCID identification number(s) for the author(s) of this article can be found under https://doi.org/10.1002/admi.202400894

© 2024 The Author(s). Advanced Materials Interfaces published by Wiley-VCH GmbH. This is an open access article under the terms of the Creative Commons Attribution License, which permits use, distribution and reproduction in any medium, provided the original work is properly cited.

DOI: 10.1002/admi.202400894

material via CVD on single-crystal metal substrates. Then, using conventional techniques involving polymethyl methacrylate (PMMA) coating and etching the metal substrate, they transfer the 2D material onto silicon.[15] Nevertheless, growing 2D materials directly on other substrates and transferring them to silicon introduces challenges in the photodetector fabrication process. The transfer process involves introducing impurities at the interface, which can hinder an effective functionality of the desired electrical junction, mainly due to the presence of the polymer residues and scattering of the charge carriers by the impurities. In addition, PMMA residues consistently affect the Fermi level of the 2D material, directly impacting the photodetector performance. The direct growth of 2D materials on silicon has not been reported so far. In this work, we report, for the first time, the direct growth of χ_3-phase borophene on silicon and demonstrate that this structure represents one of the most efficient types of electrical junctions for optoelectronic applications.

Borophene, a 2D monolayer of boron atoms with diverse applications,[16–20] poses significant challenges for its synthesis. The existing methods often yield borophene with a heterogeneous thickness, a poor quality, or a small size. Moreover, some methods necessitate costly or incompatible substrates, extreme vacuum conditions,[21,22] or lead to thick structures.[23] Therefore, an improved synthesis method is essential to investigate the intimate properties and the potential of borophene. Recently, the growth of atomically-thick borophene sheets has been performed by some of us by employing diborane (B_2H_6) pyrolysis in a CVD chamber.[15] This method produces monolayer borophene that can be transferred to different substrates, enabling empirical studies on borophene electrical and optical properties and fabrication of electronic devices.

Borophene, in comparison to graphene, possesses unique properties that have led scientists to conclude that it could be an excellent alternative for graphene in future device applications. Similar to graphene, borophene exhibits excellent electrical conductivity and superior thermal properties.[24,25] Additionally, it is theoretically predicted to exhibit superconductivity.[26] Compared to graphene, borophene also exhibits high flexibility and a higher stiffness-to-weight ratio.[27] One remarkable feature of borophene is its ability to catalyze the decomposition of molecular hydrogen into hydrogen ions and water into hydrogen and oxygen ions. This property, coupled with its lightweight nature, positions borophene as a hopeful contender for constructing supercapacitors and batteries.[16] Recent studies have highlighted the anisotropic memristor behavior of borophene.[28] These findings reveal that borophene sheets exhibit volatile memory behavior in the vertical direction and non-volatile memory behavior in the planar direction. This dual behavior significantly broadens the potential applications of borophene-based memories, particularly in information storage and in-memory computing. The stability challenge of borophene has also been overcome, making it suitable for future applications in electronic devices.[29]

Recently, we have observed anisotropic optical properties along with the excitation of in-plane hyperbolic polaritons in free-standing χ_3-phase borophene.[30] These findings indicate that borophene has promising optoelectronic applications. Based on these findings, we create here high-quality vertical Schottky junctions between χ_3 borophene and silicon for the fabrication of photodetectors with an excellent figure of merit. To achieve this objective, we employ a specific technique for borophene growth using the CVD method, which will be further explained in the subsequent sections. This technique enables the direct growth of χ_3 borophene on silicon, which is crucial for creating gapless vertical contact between borophene and silicon, resulting in a perfect electrical junction. Developing this kind of junction, rather than relying on van der walls-type stacking of 2D materials, has allowed us to fabricate a high-speed and high-responsivity photodetector. Previous works on 2D/3D junctions typically involved transferring 2D materials onto the surface of 3D materials. This transfer process often introduces unwanted residues at the 2D/3D interface, leading to electrical junctions with suboptimal performance and ideality. Our findings demonstrate that the direct growth of χ_3 borophene with exceptional optoelectrical properties on n-type silicon creates a promising electrical junction for photodetection. The photodetector based on this junction achieves an exceptionally high responsivity ranging from 260–2700 mA W^{-1} across a broad spectrum of 365–1025 nm. This performance surpasses previously reported boron-based photodetectors.

2. Results and Discussions

2.1. CVD Growth and Characterization

The fabrication process of the photodetector based on the direct growth of the borophene on silicon will be discussed in the Experimental Section in more details. **Figure 1a** (left to right) schematically illustrates the evolution of borophene growth from lithographically defined edge regions toward the silicon area, forming a borophene/Si junction at the photodetector's active area. Borophene begins to grow in regions containing aluminum and gradually extends to cover the square-shaped active area on silicon, which serves as the photodetector's active area. In this configuration, borophene forms a connection with silicon in one area while resting on insulating silicon oxide outside the square region. This arrangement allows making a contact to the borophene from top side and an electrical connection from the back of the silicon wafer to the silicon. Consequently, two contacts are established for the borophene/silicon Schottky junction. To characterize the fabricated structures, a comprehensive morphological and structural analyses have been performed using different techniques. First, a field-emission scanning electron microscope (FESEM) is utilized for investigating the geometry of the synthesized borophene sheets (see Figure 1f,g and **Figure 2a**). Surface morphology of the borophene/silicon demonstrates Al aggregates (bright area) and borophene sheets (grey regions) between the Al aggregates (Figure 2a). Energy-dispersive X-ray spectroscopy (EDS) of the position marked by the red circle in Figure 2e, clearly depicts the presence of boron atoms. Trace of aluminum and oxygen are also seen in this spectrum. The scattered distribution of aluminum is attributed to the presence of aluminum traces. Additionally, the presence of oxygen traces in this spectrum can be attributed to the native oxide on silicon substrate and the partial oxidation of borophene. Moreover, EDS of the aluminum-rich aggregates marked by the blue circle shows higher atomic weights of aluminum and oxygen along with borophene. The high concentration of boron atoms on the aluminum islands is due to the top deposition of the

© 2024 The Author(s). Advanced Materials Interfaces published by Wiley-VCH GmbH

21967350, 2025, 8, Downloaded from https://advanced.onlinelibrary.wiley.com/doi/10.1002/admi.202400894 by Christian-Albrechts-Universitat zu Kiel, Wiley Online Library on [16/10/2025]. See the Terms and Conditions (https://onlinelibrary.wiley.com/terms-and-conditions) on Wiley Online Library for rules of use; OA articles are governed by the applicable Creative Commons License

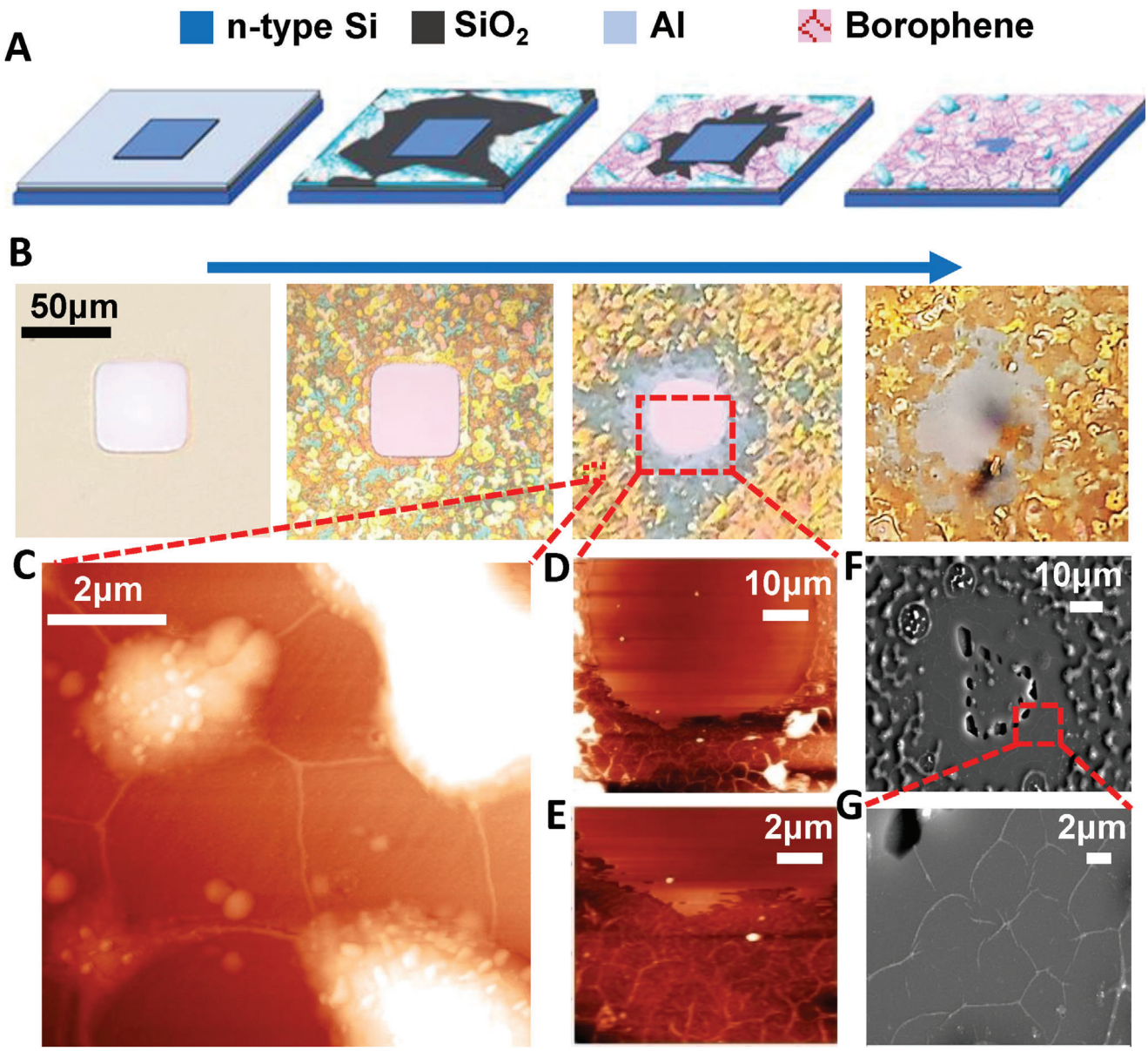

Figure 1. Direct growth of borophene on silicon and the realization of the photodetector structure. a) Schematic of the process flow starting with the deposition of SiO_2 and Al layers on silicon and photolithography of the layers to define the device active area, and following by direct growth of borophene on the prepatterned structure. During the growth step Al layer becomes aggregated. Then the borophene sheet grow from lithographically defined edge regions toward the silicon area. b) Optical images showing the Al/SiO_2/Si after photolithography (left), aggregation of Al layer at the beginning of the growth (second image), progression of borophene growth toward the silicon area (third image), and the total coverage of the silicon area (right). c–e) AFM images showing the topography of the different parts of the sample. f,g) SEM images showing the final structure of borophene–Si Schottky junction.

boron atoms. Previous reports[31] have shown that the formation of boron oxide is mainly limited to the aluminum aggregates and edges, while the borophene configuration in the area marked by the red circle remains intact. Based on first-principle density-functional theory (DFT) calculations,[31] this is due to the electronic interaction between the aluminum aggregates and the boron atoms at the edges of the borophene sheet, which can inhibit oxidation and helps to preserve the borophene sheets for extended periods. The polygonal borophene domains, separated from the Al islands by sharp edges, are highlighted by yellow dashed lines, depicting the crystalline structure of the synthesized sheets. The atomic force microscope (AFM) images in Figures 1c and 2b also illustrate the aggregation of aluminum layer into clustered islands. Moreover, it can be observed in these figures that borophene sheets have grown in the regions between the aluminum islands, and the boundaries of the interconnected borophene sheets are clearly visible in this image.

It is crucial to analyze the crystalline structure and chemical component of borophene in the silicon regions where aluminum aggregates are absent. Our previous publication extensively

 © 2024 The Author(s). Advanced Materials Interfaces published by Wiley-VCH GmbH

21967350, 2025, 8, Downloaded from https://advanced.onlinelibrary.wiley.com/doi/10.1002/admi.202400894 by Christian-Albrechts-Universitat zu Kiel, Wiley Online Library on [16/10/2025]. See the Terms and Conditions (https://onlinelibrary.wiley.com/terms-and-conditions) on Wiley Online Library for rules of use; OA articles are governed by the applicable Creative Commons License

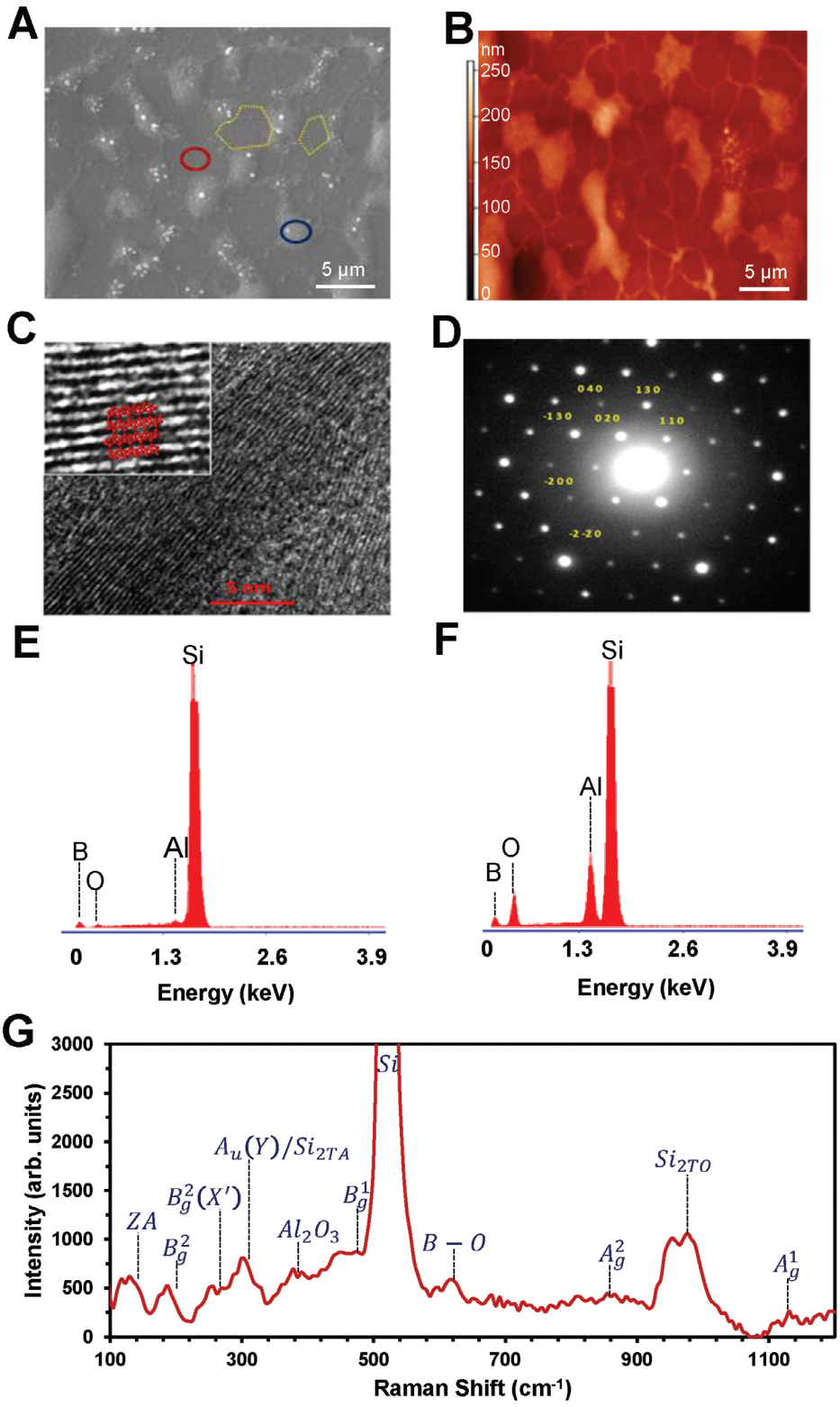

Figure 2. Morphological and structural characteristic. A) FESEM image showing the grey regions, which represent borophene sheets, and the bright areas indicating Al islands on the silicon substrate. B) AFM image illustrating the aggregation of aluminum and the borophene sheets which have grown in the regions between the aluminum islands. c) HRTEM image showing the borophene's lattice image. The inset is a magnified view of the HRTEM along with the superimposed χ_3 borophene atomic structure. D) SAED pattern with the Miller indices determined by comparing the theoretical values of the d-spacing of χ_3 borophene with a standard deviation of 0.005. E,F) EDS spectra showing the elements involved in the position marked by red (E), and blue (F) circles in panel a. G) The Raman spectra of the grown sample depicting a prominent fingerprint of the presence of the χ_3 phase borophene.

© 2024 The Author(s). Advanced Materials Interfaces published by Wiley-VCH GmbH

21967350, 2025, 8, Downloaded from https://advanced.onlinelibrary.wiley.com/doi/10.1002/admi.202400894 by Christian-Albrechts-Universitat zu Kiel, Wiley Online Library on [16/10/2025]. See the Terms and Conditions (https://onlinelibrary.wiley.com/terms-and-conditions) on Wiley Online Library for rules of use; OA articles are governed by the applicable Creative Commons License

studied the effects of aluminum and silicon substrates on borophene growth using scanning photoemission spectroscopy (SPEM).[31] Our pioneering work demonstrated that borophene growth initiates at the edges of aluminum aggregates and extends between aluminum islands. Initially, the inter-island areas were minimal, but in this study, we significantly expanded the growth area on silicon, forming the active region of the detector. SPEM analysis, as reported in our published paper,[31] reveals that borophene on silicon not only exhibits an excellent crystalline structure but also superior oxidation resistance compared to borophene on aluminum. Here, we also investigate the crystalline structure of borophene sheets grown on silicon. The borophene sheets transferred onto the copper grid were analyzed using high-resolution transmission electron microscopy (HRTEM). The images are depicted in Figure 2c, while the corresponding selected area electron diffraction (SAED) pattern is illustrated in Figure 2d.

In the HRTEM image, parallel lattice strips align excellently with the distance between parallel strip-like regions of high atomic concentration in the χ_3 phase borophene. The interstrip distances in the χ_3 phase borophene is calculated to be 4.4 angstroms. The inset of Figure 2c contains a magnified view of the HRTEM along with the superimposed χ_3 borophene atomic structure. Additionally, we have observed a remarkable consistency between the obtained diffraction pattern and the primary reciprocal lattice of χ_3 borophene. The Miller indices related to the observed diffraction pattern are provided in Figure 2d. These Miller indices are determined by comparing the theoretical values obtained from the real-space interplanar spacings with a standard deviation of 0.005.

The Raman spectra of the grown sample provided in Figure 2e reveals a prominent fingerprint of the presence of the χ_3 phase borophene in the sample. The spectrum predominantly exhibits surface B–B vibrations at (B_g^2(176 cm^{-1}), $B_g^2(X')$ (240 cm^{-1}), $A_u(Y)$ (305 cm^{-1}), B_g^1(425 cm^{-1}), and A_g^1 (1135 cm^{-1}), consistent with previous reports of Raman spectra for the χ_3 phase.[16,32] Unlike graphene, borophene is anisotropic, lacking identical symmetry axes, which results in the splitting of the scattering modes and consequently it leads to an increase in the number of Raman peaks. Another peak at around A^2_g (865 cm^{-1}) indicates the presence of a small amount of the β_{12} borophene phase. Furthermore, since silicon is used as a substrate for the growth, a main silicon peak is clearly observable at around 520 and 940 cm^{-1}. The presence of alumina and boron oxide is identified at 375 and 620 cm^{-1}, respectively.

2.2. Optoelectrical Measurements of Borophene/Silicon Photodetector

Schematic diagram of the borophene/silicon-based photodetector is illustrated in **Figure** 3a and the mechanism of the process through which the χ_3 borophene/Si Schottky junction detects light using the photovoltaic effect is depicted in Figure 3b. The Schottky barrier height created at the interface of the χ_3 borophene/Si Schottky junction is obtained as the difference between the work function of χ_3 borophene, ϕ_B, and the electron affinity of the n-type silicon, χ_{Si}. When the χ_3 borophene/Si Schottky junction absorbs incident photons, it generates electron–hole pairs, resulting in an increase in carriers. These carriers are to be separated under an external reverse bias to generate photocurrent. To determine the band structure and band-bending at the borophene–silicon junction, DFT calculation is utilized (see Experimental Section). In this method, a slab model of the material is constructed in a super-cell approach, including a sufficiently thick vacuum region to avoid interactions between periodic images. After optimizing the geometry of χ_3 borophene, the electrostatic potential is calculated along the direction perpendicular to the surface. The vacuum level is determined by identifying the flat region of the electrostatic potential far from the surface. The work function is then obtained by subtracting the Fermi energy of the material, derived from the DFT calculation, from the vacuum level. Considering the work function of χ_3-borophene as 4.83 eV (determined via DFT calculations in Figure S1, Supporting Information, and confirmed experimentally in Figure S4, Supporting Information) and the electron affinity of the n-type silicon under study as 4.05 eV,[33] the Schottky barrier height is estimated to be 0.78 eV.

To evaluate the rectifying behavior and the charge transport across the χ_3 borophene/Si vertical junction, the $I-V$ characteristic of the junction is investigated in a dark room (Figure 3c). Considering the thermionic emission mechanism for this junction, which is typically dominant for van der Waals junctions between 2D materials and silicon at temperatures above room temperature,[14] the current density through the junction can be expressed as follows

$$J = A^* T^2 e^{-\frac{\phi_b}{k_B T}} \left(e^{\frac{e \times V}{\eta k_B T}} - 1 \right) \quad (1)$$

where A^*, T, ϕ_b, and η are the Richardson constant, the temperature, the Schottky barrier height, and the ideality factor, respectively. In this equation, V represents the voltage directly applied to the junction and can be expressed as $V_E - IR_s$, where V_E is the externally applied voltage, I denotes the current passing through the junction, and R_s signifies the series resistance. By fitting Equation (1) to the $I-V$ characteristics of the junction in the absence of light (Figure 3c), we can determine A^*, η, ϕ_b, and R_s as follows: $A^* = 133$ A $cm^{-2}K^{-2}$, $\eta = 3.68$, $\phi_b = 0.78$ eV, and $R_s = 2.25$ kΩ.

According to the DFT calculations (see Figure S1, Supporting Information), χ_3 borophene exhibits anisotropic electronic behavior. The crystal structure of χ_3 borophene (Figure S1a, Supporting Information) has some strip-like regions of high atomic concentration parallel to the crystallographic y-direction, which make the electronic behavior of χ_3 borophene anisotropic. The band structure of χ_3 borophene obtained by DFT calculation is provided in Figure S1b (Supporting Information). This electronic band structure depicts the distinct anisotropy of χ_3 borophene. In certain directions, such as M–X, the electron bands near the Fermi level are relatively flat, suggesting more localized electronic states and directional variation in electronic properties (Figure S1c, Supporting Information). In contrast, the electron energy bands through the direction such as N–Y cross the Fermi level, indicating metallic behavior (Figure S1d, Supporting Information). Therefore, χ_3 borophene exhibits metallic behavior with strong anisotropy, and the electrical conductivity is confined along the atomic strips parallel to the Y direction. The

© 2024 The Author(s). Advanced Materials Interfaces published by Wiley-VCH GmbH

21967350, 2025, 8, Downloaded from https://advanced.onlinelibrary.wiley.com/doi/10.1002/admi.202400894 by Christian-Albrechts-Universitat zu Kiel, Wiley Online Library on [16/10/2025]. See the Terms and Conditions (https://onlinelibrary.wiley.com/terms-and-conditions) on Wiley Online Library for rules of use; OA articles are governed by the applicable Creative Commons License

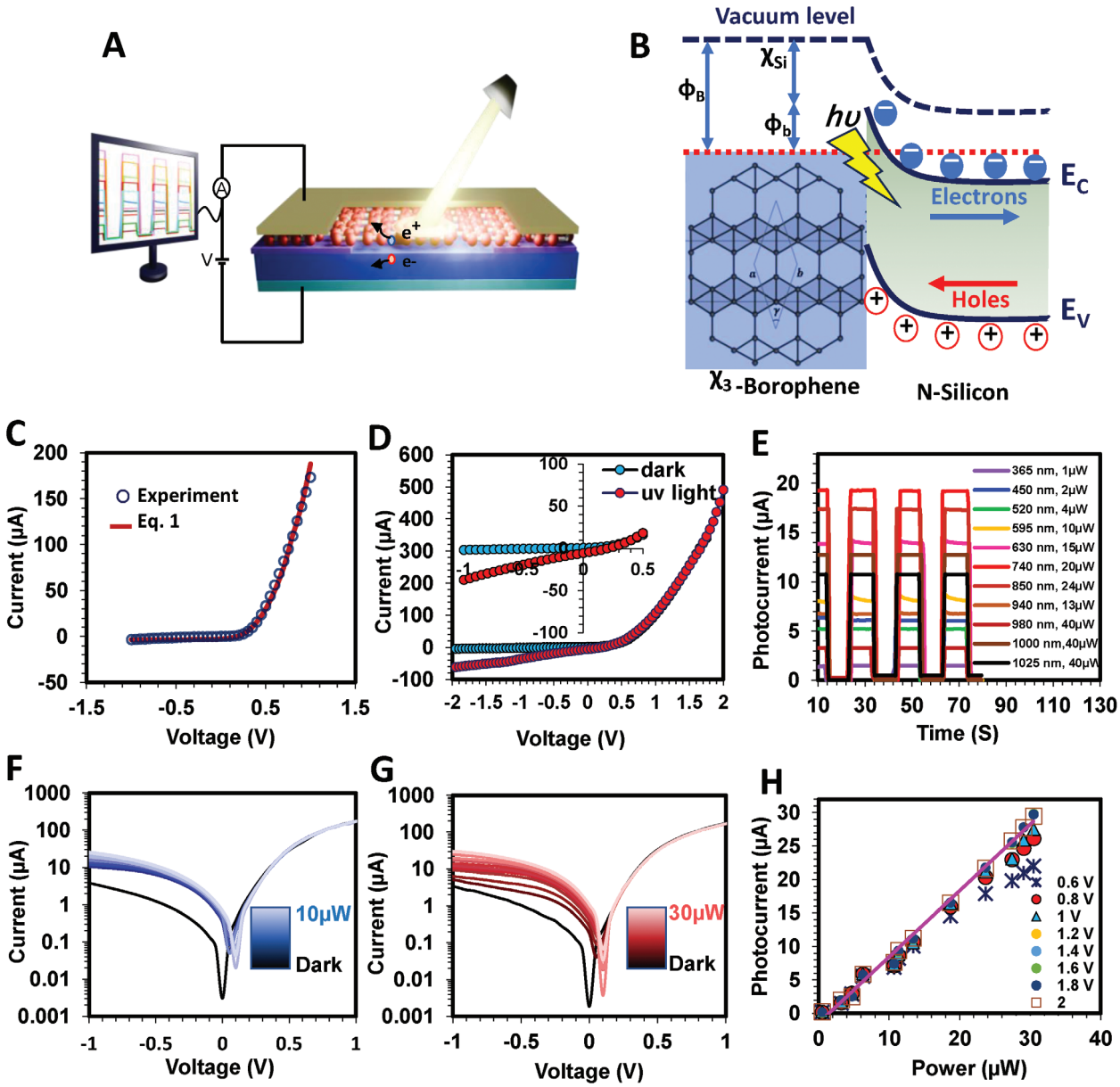

Figure 3. Optoelectrical characteristics of the $\chi 3$ borophene/silicon-based photodetector. A) Schematic representation of the $\chi 3$ borophene/Si photodiode and the measurement setup. B) Diagram showing the formation of Schottky junction at the interface of $\chi 3$ borophene/silicon. The Schottky barrier height created at the interface of the $\chi 3$ borophene/Si Schottky junction is obtained as the difference between the work function of $\chi 3$ borophene, ϕ_B, and the electron affinity of the n-type silicon, χ_{Si}. The generated electron–hole pairs are separated by the interface's electric field, leading to the injection of holes into borophene and electrons toward silicon. C) *I* –*V* characteristic of the junction in the absence of optical radiation (dark I–V curve) and the corresponding fitted curve according to Equation (1). D) The *I* –*V* characteristic of the junction under UV light, compared to the dark *I*–*V* curve, demonstrating a transition from a rectifying behavior to an almost linear behavior. E) Real-time optical responses of the detector under varying illumination wavelengths and power levels. F) Semi-logarithmic *I*–*V* characteristic of the detector under different intensities of 450 nm illumination. G) Semi-logarithmic *I*–*V* characteristic of the detector under different intensities of 740 nm illumination. H) Photocurrent versus incident power at different reverse bias voltages under 740 nm illumination showing the linear behavior at higher voltages.

calculated permittivity of χ_3 borophene, shown in Figure S1e,f (Supporting Information), confirms that the real part of the permittivity along the *y*-direction, $\mathrm{Re}(\epsilon_{yy})$, becomes negative, indicating the metallic behavior. The important feature of Figure S1e (Supporting Information), is that the permittivity is near zero at the wavelengths ≈450 nm. It means that above this wavelength χ_3 borophene is metallic, and below this, it behaves as a non-metallic material. The evidence for this important behavior is provided in Figure 3d. As shown in this figure, the *I*–*V* characteristic of the χ_3 borophene/silicon junction under UV light illumination changes to an almost linear characteristic like an Ohmic junction.

To assess the performance of the χ_3 borophene/Si photodetector, the time-resolved response of the detector is evaluated.

© 2024 The Author(s). Advanced Materials Interfaces published by Wiley-VCH GmbH

21967350, 2025, 8, Downloaded from https://advanced.onlinelibrary.wiley.com/doi/10.1002/admi.202400894 by Christian-Albrechts-Universitat zu Kiel, Wiley Online Library on [16/10/2025]. See the Terms and Conditions (https://onlinelibrary.wiley.com/terms-and-conditions) on Wiley Online Library for rules of use; OA articles are governed by the applicable Creative Commons License

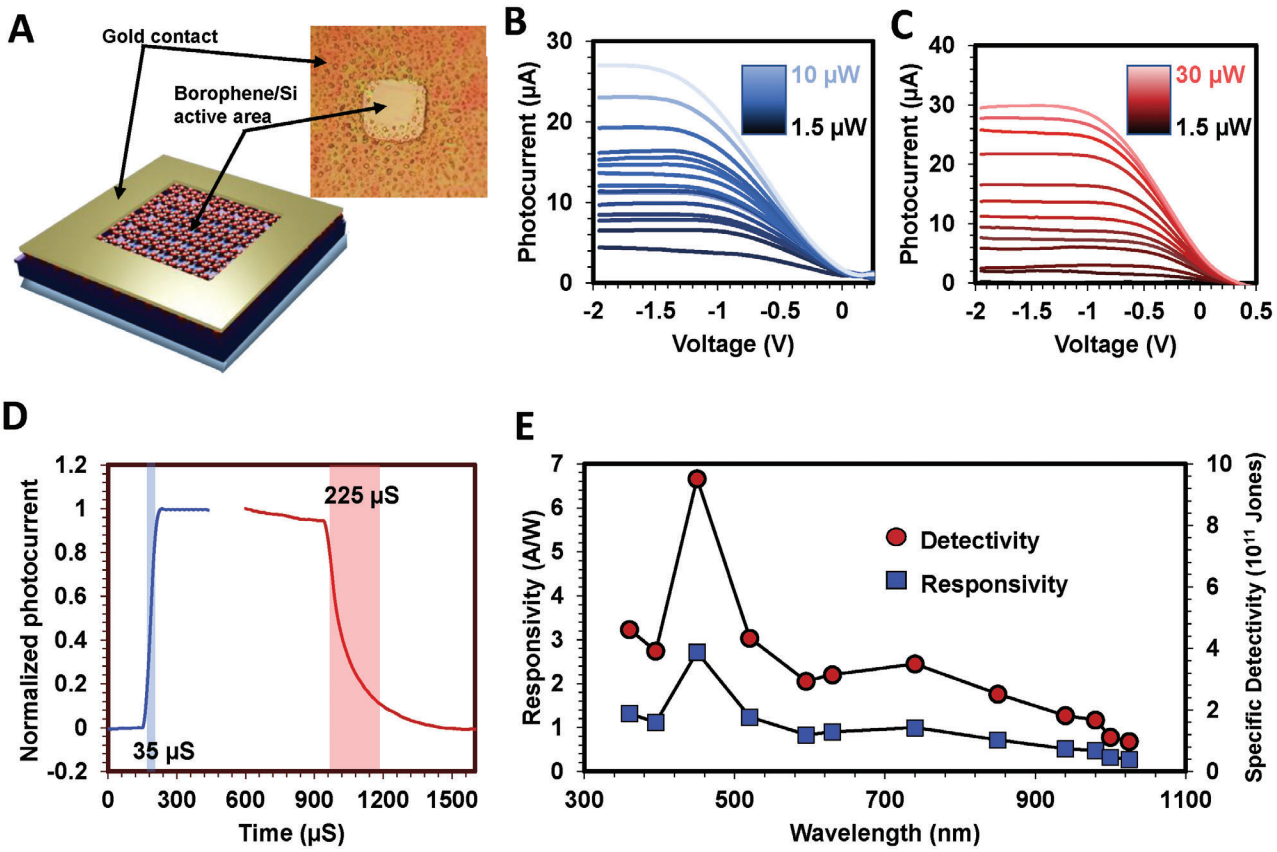

Figure 4. Photodetection figures of merit of the χ_3 borophene/silicon junction. A) Schematic and optical image of the device under study. Photocurrent versus bias voltage for the different power of B) 450 nm and C) 740 nm illumination. D) χ_3 Borophene/silicon photodetector's response time. E) Detectivity and responsivity of the χ_3 borophene/Si photodetector under revere-bias voltage of 1 V across a broad range of wavelengths from UV–vis to IR, showing a peak at around ENZ.

Rapid and consistent light responsiveness plays a crucial role in optimizing the performance of photodetectors for practical applications. In Figure 3e, real-time optical responses of the device are depicted under varying illumination wavelengths and power levels. The photo response of the χ_3 borophene–Si photodetector illustrated in Figure 3e, demonstrates cyclic on-and-off switching of illumination over a 10-s duty cycle under a 1 V reverse bias. Various LED light sources, ranging from ultraviolet to infrared with wavelengths of 365, 460, 520, 595, 630, 740, 850, 940, 980, 1000, and 1025 nm, are employed for illumination. Notably, discernible photoelectric response is observed across all LED illuminations with different wavelengths. This response over such a wide range of wavelengths indicates an exceptionally broad band responsivity in this type of detector which has not been reported in similar detectors made with 2D materials so far.

Next, we study the χ_3 borophene–silicon photodetector's $I-V$ characteristics at various irradiance levels and compared it with its dark current. These measurements are conducted at all mentioned wavelengths. Figure 3f,g illustrates the measured output $I-V$ characteristic at wavelengths of 450 and 740 nm, respectively. As depicted in Figure 3f,g, with increasing light intensity, the photocurrent intensity increases. The rectification ratio of the diode, which is defined as $RR = |I_{\text{forward}}/I_{\text{reverse}}|$ at 1 V, is around 51. The effective rectifying behavior confirms the establishment of an exceptionally high-quality electrical junction through the direct growth of borophene on silicon, positioning it as a promising candidate for electronic devices. According to the results of Figure 3f, the rectifying ratio drops to 6.5 with 10 μW of light at 450 nm. At 740 nm, the ratio at the same light intensity drops to 16.5. These big changes at very low light levels, highlight the high sensitivity of the χ_3 borophene–silicon photodetector.

Figure 3h illustrates the photocurrent ($I_{\text{PC}} = I_{\text{Light}} - I_{\text{Dark}}$) as a function of incident light intensity. Since photocurrent changes with bias voltage, we display the photocurrent at various voltage levels. In this plot, it is evident that at lower bias voltages, the photocurrent saturates with increasing the optical powers. However, as the reverse bias climbs to 1 V and beyond, the saturation region gradually diminishes, leading to a linear variation in photocurrent across all tested intensities. Consequently, the linear dynamic range (LDR $= 20\log(P_{\max}/P_{\min})$) expands from 18.7 dB at zero bias to 26 dB at $V_b = -1$ V. Notably, bias voltage serves as an effective means to modulate photocurrent at higher optical powers. Moreover, utilizing the same dataset, the differential photocurrent responsivity of the detector is determined by assessing the slope of the photocurrent versus intensity.

The photodetection figures of merit of the χ_3 borophene/silicon junction (**Figure** 4a) are collected in Figure 4. In panel b and c of this figure, the photocurrent is plotted against

© 2024 The Author(s). Advanced Materials Interfaces published by Wiley-VCH GmbH

21967350, 2025, 8, Downloaded from https://advanced.onlinelibrary.wiley.com/doi/10.1002/admi.202400894 by Christian-Albrechts-Universitat zu Kiel, Wiley Online Library on [16/10/2025]. See the Terms and Conditions (https://onlinelibrary.wiley.com/terms-and-conditions) on Wiley Online Library for rules of use; OA articles are governed by the applicable Creative Commons License

Table 1. Comparison between the optoelectronic parameters of the fabricated photodetector with the reported boron-based photodetectors.

Materials	Spectral range [nm]	Best Responsivity [A/W]	Detectivity [$\times 10^{11}$ Jones]	Response time [ms]	Refs.
B_{12}-borophene/Si	365–850	0.48	4.39	115	[17]
Boron	365–700	91.7×10^{-6}	$\mathbf{1.6 \times 10^{-3}}$	1800	[38]
α-borophene/Mica	400–700	1.04	1.27	400	[18]
$\delta_5 - \frac{\text{borophene}}{\text{n}} -$ **zinc oxide**	365	0.102	1.43×10^{-2}	2800	[39]
$\alpha' - 4\mathbf{H} -$ **borophene** on gallium arsenide	940	31×10^{-5}	10^{-3}	117	[40]
χ_3-borophene/Si (direct growth)	365–1025	2.7	9.3	0.035	This work

bias voltage. We assessed the photoelectric characteristics under illumination of 450 and 740 nm LEDs at varying power intensities. The photocurrent exhibits a notable increase with rising intensity, a trend attributed to the increased generation of photogenerated carriers. At a constant light intensity, the photocurrent initially rises as the bias voltage increases, eventually reaching a saturated plateau at higher reverse voltages. Increasing the reverse bias voltage expands the depletion region width, facilitating the collection of photogenerated carriers.

To assess the device's broad-spectrum sensitivity, Figure 4e illustrates the detectivity and responsivity of the photodetector. At 450 nm, the detector achieves peak values of 2.7 A W^{-1} for responsivity and 9.8×10^{11} Jones for detectivity. Several factors contribute to the high responsivity and internal quantum efficiency exceeding 100% in the borophene/silicon detector. The borophene/Si junction forms an ultra-shallow junction, ideal for detecting light absorbed near the Si surface, generating charges close to the silicon surface. This junction reduces the diffusion path and prevents rigorous surface recombination typical in traditional junctions, leading to high responsivity. Additionally, borophene's unique absorption property at 450 nm results in a long carrier lifetime for hot electrons, contributing to the photocurrent or potential carrier multiplication, thereby boosting internal quantum efficiency beyond 100%.

The quantum efficiency exceeding 100% in the borophene/silicon photodetector suggests electronic gain consistent with a photoconductive gain mechanism.[34] This mechanism is fundamentally achieved by preventing recombination, allowing carriers to pass over the circuit multiple times. The low recombination rate in the borophene/silicon junction is due to the higher conductivity of borophene compared to silicon. Injected electrons in the silicon layer transport slowly due to lower charge mobility and diffusivity, influenced by localized states from dopants. Conversely, the borophene sheet's high conductivity allows injected holes to rapidly transit to the electrodes. This results in electrons being trapped in long-lived, localized states in silicon, while hole carriers flow freely through borophene, leading to photoconductive gain. This gain can be expressed as $G = \frac{\tau}{\tau_t}$, where τ is the average time spent by trapped electrons, and τ_t is the average transit time for free-flowing carriers through borophene. The responsivity of borophene/silicon detector decrease as the wavelength increases, reaching 260 mA W^{-1} and 9.5×10^{10} Jones at 1025 nm. The exceptionally high responsivity ranging from 260–2700 mA W^{-1} across this wide spectrum, attained by the χ_3 borophene–silicon photodetector, surpasses previously reported boron-based detector performance (**Table 1**) by approximately an order of magnitude. This enhanced responsivity enables satisfactory performance even at higher wavelengths up to 1025 nm, a range where borophene and silicon traditionally exhibit low absorption efficiency. According to Figure 4e, the responsivity shows a peak around 450 nm which is matched with the epsilon-near–zero (ENZ)[35] region of the χ_3 borophene. As discussed before, the metallic behavior of the χ_3 borophene arises from the permittivity along the *y*-direction. Consequently, ENZ wavelength is the wavelength at which the real part of the permittivity along *y*-direction becomes near zero. Furthermore, at the ENZ wavelength the absorption rate of the electromagnetic energy in the material is enhanced due to the dissipation, leading to significant light absorption.[35,36] The plasma energy in materials aligns with the wavelength at which the permittivity approaches zero, whereas surface plasmon resonances occur when the permittivity is equal to −1.[37] This enhanced absorption at around ENZ wavelengths results in a significant enhancement in the responsivity of the χ_3 borophene/silicon junction.

One of the crucial aspects of photodetectors is their response time, reflecting how quickly a detector reacts to an excitation. In Figure 4d the photodetector's response time is illustrated for the χ_3 borophene/silicon photodetector. Calculated rise times ($\tau_r = \tau_{90\%} - \tau_{10\%}$) and fall times ($\tau_f = \tau_{10\%} - \tau_{90\%}$) are 35 and 225 µs, respectively. The efficient separation and collection of photogenerated carriers at the Schottky junction interface are essential. This fast response and low recovery time are indicative of a low trap concentration, attributed to the direct growth of borophene on silicon and the rapid release of trapped electrons from vacancies and trapped states (See Table 1 for comparison). These findings suggest that employing direct borophene growth on silicon enhances the quick and efficient separation and collection of photogenerated electron–hole pairs, crucial for monitoring ultrafast optical signals.

2.3. Investigation of the Origin of Responsivity Peak via CL Analysis

To analyze the χ_3 borophene as a metallic 2D material and to investigate the origin of the peak responsivity observed in Figure 4e, we conducted spectrally and spatially resolved cathodoluminescence (CL) spectroscopy measurements on χ_3 borophene sheets

© 2024 The Author(s). Advanced Materials Interfaces published by Wiley-VCH GmbH

21967350, 2025, 8, Downloaded from https://advanced.onlinelibrary.wiley.com/doi/10.1002/admi.202400894 by Christian-Albrechts-Universitat zu Kiel, Wiley Online Library on [16/10/2025]. See the Terms and Conditions (https://onlinelibrary.wiley.com/terms-and-conditions) on Wiley Online Library for rules of use; OA articles are governed by the applicable Creative Commons License

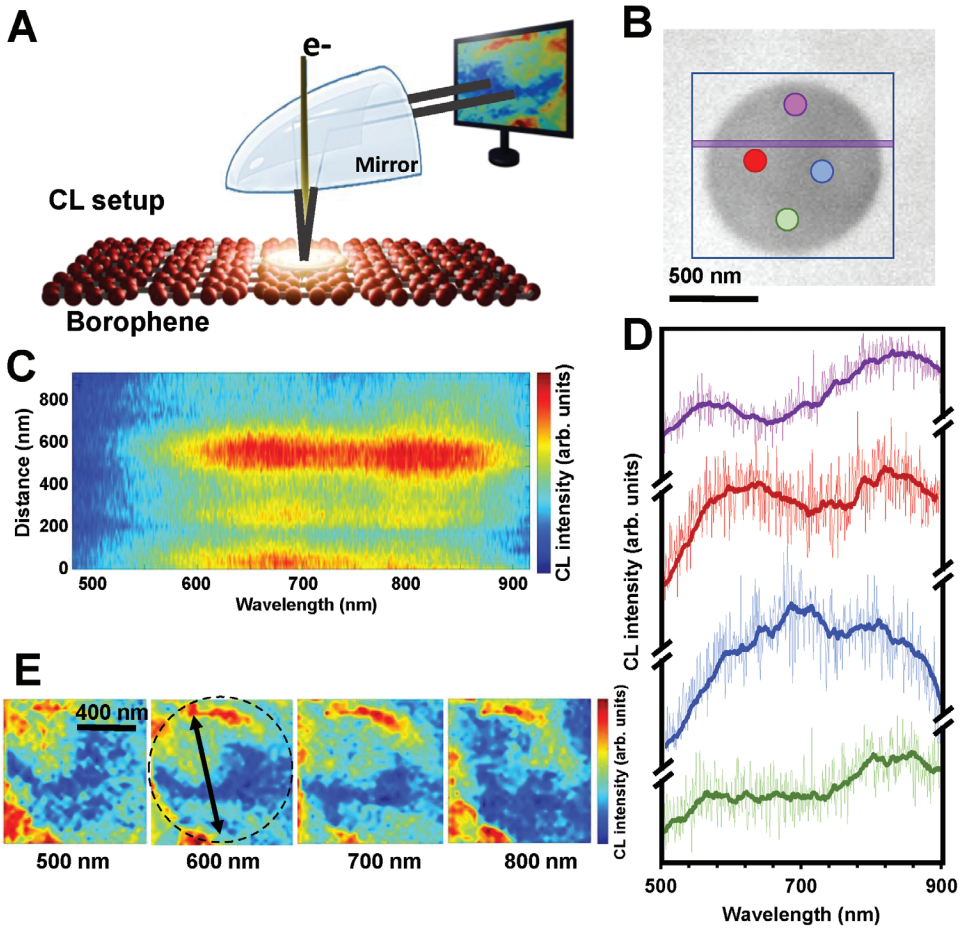

Figure 5. Cathodoluminescence measurements. A) Experimental setup featuring a CL mirror and the radiation emitted from the borophene, that is gathered using a parabolic mirror and sent to the analyzing path. B) SEM image of the sample under study. C) Wavelength–distance CL intensity maps, acquired along the scanning directions of purple ribbon shown in panel b. D) CL spectrum extracted from the location marked by the colored dots in panel b. E) CL hyperspectral image at depicted wavelengths showing the anisotropic propagation of the hyperbolic surface plasmon polariton.

transferred onto a holey gold substrate (**Figure** 5b). CL spectroscopy is chosen due to its ability to capture the highly confined plasmonic response of borophene flakes, due its high-spatial resolution of 1 nm.[30,41–43] A holey gold substrate is used to avoid charging caused by the penetration of the electron beam into the nonconducting silicon substrate and the incoherent CL response caused by silicon.[44] The analysis here can demonstrate the broadband plasmonic response of borophene. The details of the CL experiment, schematically shown in Figure 5a, are discussed in the Experimental Section. The excitation of in-plane polaritons at the different wavelengths can be seen in Figure 5e. As expected from the DFT calculations, anisotropy can be observed in the CL map, confirming the propagation of in-plane plasmon–polaritons in a specific direction (indicated by the black arrow in Figure 5e). The CL spectra within the wavelength range of 500 to 900 nm and acquired from various positions marked by colored dots and the purple ribbon in Figure 5b, are provided in Figures 5c,d respectively. The main CL peaks are located at 550 and 800 nm. The bulk plasmon energy is ≈450 nm (according to Figure S1e, Supporting Information), and therefore CL signal is enhanced at all wavelengths longer than this wavelength, due to the excitation of plasmon polaritons. The wavelength at which the permittivity of a metal is zero (the bulk plasmon wavelength) is typically shorter than the wavelength of our CL detector; nevertheless, surface plasmon resonances associated to the localized plasmon resonances of borophene confined in the hole geometry is perfectly captured.

Due to the plasmonic behavior of the χ_3 borophene, maximum light absorption occurs at the wavelength where the permittivity of borophene in the metallic direction approaches zero. At longer wavelength, plasmon polaritons are excited and the electric field intensity within the borophene layer is enhanced, forming short-range hyperbolic surface plasmon polaritons. These polaritons have a strongly dissipative nature as well up to the wavelength of ≈1050 nm. Consequently, the responsivity peak at 450 nm arises from the enhanced light absorption caused by bulk plasmon excitations. However, for wavelengths shorter than 450 nm, the real part of the permittivity becomes positive, leading to nonmetallic behavior. As a result, the Schottky junction at the χ_3 borophene/silicon interface disappears, causing a loss in the efficient collection of photogenerated electrons.

© 2024 The Author(s). Advanced Materials Interfaces published by Wiley-VCH GmbH

21967350, 2025, 8, Downloaded from https://advanced.onlinelibrary.wiley.com/doi/10.1002/admi.202400894 by Christian-Albrechts-Universitat zu Kiel, Wiley Online Library on [16/10/2025]. See the Terms and Conditions (https://onlinelibrary.wiley.com/terms-and-conditions) on Wiley Online Library for rules of use; OA articles are governed by the applicable Creative Commons License

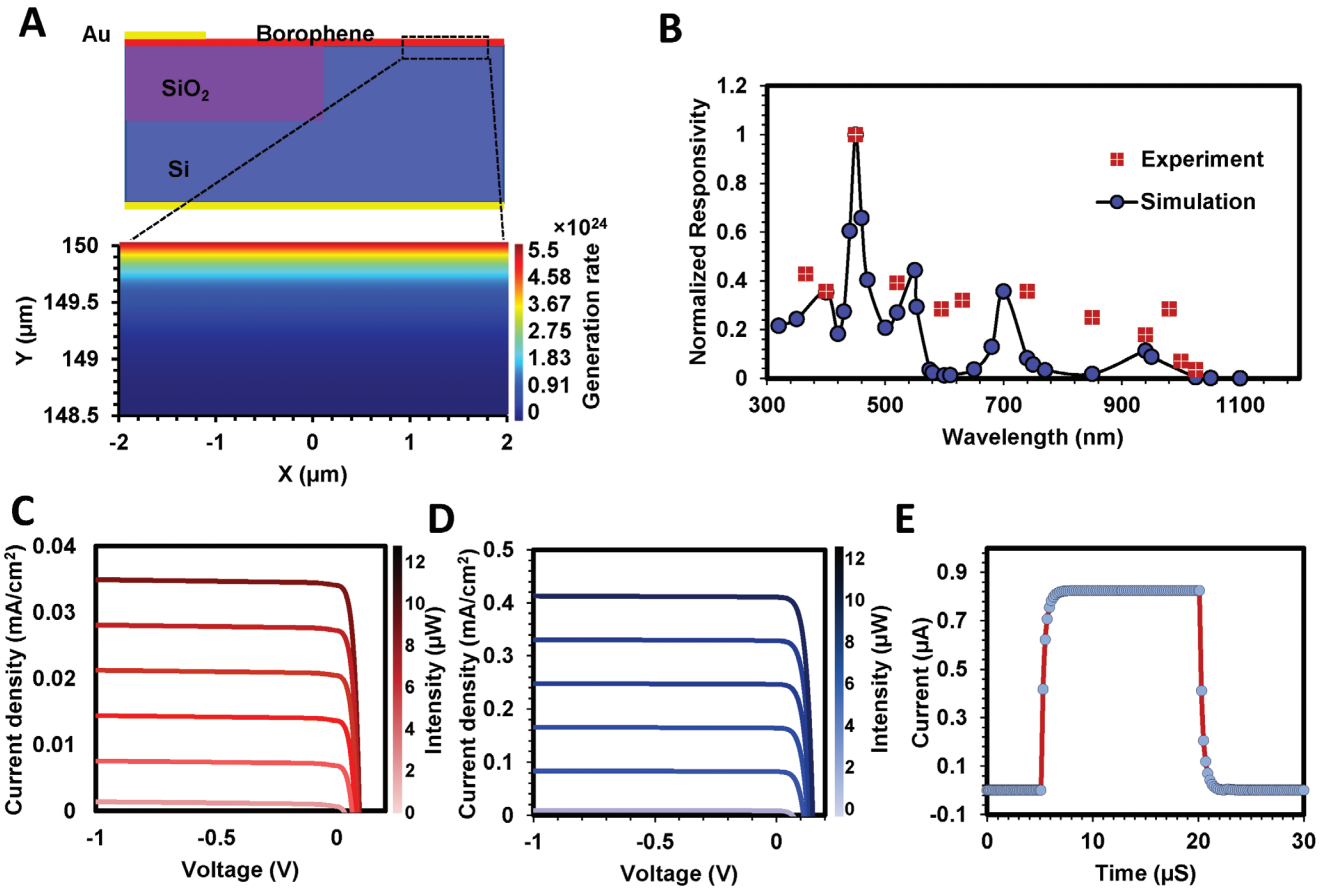

Figure 6. FDTD simulation results. A) Carrier generation rate profile (below) of the device under study (top) extracted from FDTD for $\lambda = 450$ nm. B) Comparison between the normalized responsivities of the χ_3 borophene/Si-based photodetector obtained by simulation and experiment. Photocurrent density versus reverse-bias voltage obtained by the simulation for C) 450 nm, and D) 740 nm illuminations. E) Response time of the photodetector obtained by the simulation.

2.4. FDTD Simulation of the Responsivity

When light hits the $\chi 3$ borophene/Si sample, it is predominantly absorbed by the silicon, with some absorption also occurring in the borophene sheet. The absorption power density can be determined using the following equation

$$P_{\text{abs}} = \frac{1}{2}\,\omega\left|\vec{E}\right|^2 Im\{\varepsilon\} \tag{2}$$

where, $\vec{E}$ is electric field, ω is the angular frequency of the incident light, and ϵ represents the permittivity at a given frequency ω. By utilizing the permittivity of the χ_3 borophene obtained with DFT calculations, and solving Maxwell's equations for the χ_3 borophene/Si configuration using the finite-difference time-domain (FDTD) method, the density of photon absorption rate can be calculated from the above equation as

$$G = \frac{P_{\text{abs}}}{h\nu} \tag{3}$$

By integrating the resulting photon rate over the simulation spectrum and assuming perfect quantum efficiency, the electron–hole generation rate can be determined (see the profile in **Figure** 6a).

The separation of electrons and holes at the interface of χ_3 borophene/Si leads to free electrons and holes with concentrations n, and p, respectively, which are equal ($n = p$). The $I-V$ characteristics of the $\chi 3$ borophene/Si junction is obtained using the Poisson and drift-diffusion equations. First, we solve for the Poisson's equation to obtain the potential distribution (V) within the structure and the carrier density distribution (ρ) using

$$-\nabla \cdot (\varepsilon \nabla V) = e\rho, \tag{4}$$

In the second step, the current density distributions for both electrons (J_{n}) and holes (J_{p}) are obtained as

$$J_{\text{n}} = e\mu_{\text{n}}\rho \boldsymbol{E} + eD_{\text{n}}\nabla\rho, \tag{5}$$

and

$$J_{\text{p}} = e\mu_{\text{p}}\rho \boldsymbol{E} - eD_{\text{p}}\nabla\rho, \tag{6}$$

where e is the elementary charge and, μ_{n} and μ_{p} are the mobility of electrons and holes, respectively. D_{n}, and D_{p} are the diffusion

© 2024 The Author(s). Advanced Materials Interfaces published by Wiley-VCH GmbH

21967350, 2025, 8, Downloaded from https://advanced.onlinelibrary.wiley.com/doi/10.1002/admi.202400894 by Christian-Albrechts-Universitat zu Kiel, Wiley Online Library on [16/10/2025]. See the Terms and Conditions (https://onlinelibrary.wiley.com/terms-and-conditions) on Wiley Online Library for rules of use; OA articles are governed by the applicable Creative Commons License

21967350, 2025, 8, Downloaded from https://advanced.onlinelibrary.wiley.com/doi/10.1002/admi.202400894 by Christian-Albrechts-Universitat zu Kiel, Wiley Online Library on [16/10/2025]. See the Terms and Conditions (https://onlinelibrary.wiley.com/terms-and-conditions) on Wiley Online Library for rules of use; OA articles are governed by the applicable Creative Commons License

coefficient of electrons and holes, respectively.[45,46] The total current is finally obtained as $J = J_n + J_p$.

The electrostatic properties of the device across a bias voltage range of −1 to 1 volts under both dark conditions and illumination are simulated in this study. Rigorous testing of the simulations is conducted across diverse parameters to ensure result reliability. Based on these simulations, we determined the responsivity of the junction and compared it with experimental results (Figure 6b). The responsivity of the device depends on its active area, but due to limitations in the size of the simulation domain, we normalized the responsivity to the highest value at 450 nm. The comparison revealed that this normalized responsivity peaks around 450 nm and decreases to zero for wavelengths above 1025 nm, consistent with experimental findings. The responsivity approaches zero at longer wavelengths due to the vanishing of the surface plasmon polaritons at wavelengths longer than 1050 nm (Figure S2, Supporting Information), as well as the negligible material absorption at those wavelengths. Therefore, the responsibility of the photodetector at the wavelength ranges between 300 and 1050 nm is affected by two processes, namely, the material absorption and surface plasmon polariton excitation, resulting in the fluctuating photoresponsivity efficiency versus the wavelength of the incoming light.

To further validate our results, we compared the photocurrent density versus applied reverse-bias voltage obtained from simulations for 450 and 740 nm illumination (Figures 6c,d respectively). According to the simulation results, the photocurrent densities at 10 μW intensity are 0.415 mA cm^{-2} (450 nm) and 0.035 mA cm^{-2} (740 nm), while experimental values for a device with a 0.04 cm^2 active area are 0.675 and 0.25 mA cm^{-2}, respectively. Some of the discrepancies between theoretical and experimental results arise from the fact that the assigned wavelengths for experimental data correspond to the peak of the LED optical spectrum, while LEDs typically have a spectral bandwidth of ≈50 nm (full wave half maximum). For example, the experimental responsivity value at $\lambda = 740$ nm is approximately equal to simulation's normalized responsivity value at $\lambda = 700$ nm. Notably, the responsivity for longer wavelengths is nearly an order of magnitude higher than predicted for monolayer and pure borophene on silicon. This can be associated with the existence of grain boundaries and strains in the practical device, leading to further enhancement of the light absorption.

Another important characteristic of the photodetector is its response time (Figure 4d). The simulation results, which are illustrated in Figure 6e, show that the predicted response time is ≈2.5 μs, which is one order of magnitude smaller than the rise time obtained in the experiment and two orders of magnitude smaller than the fall time. Although the response time of the fabricated detector is much better compared to similar reported detectors[15,17,18] that mainly exhibit response times in the range of milliseconds, simulations indicate that there is still room for improving the response speed for such a structure. It is still possible to enhance the response time by reducing impurities and defects. However, the presence of a small amount of impurities, which may lead to higher sensitivity and the generation of color centers, could be beneficial for the high sensitivity of this detector, even if it slightly increases the response time.

3. Conclusion

The direct growth of 2D χ_3 borophene on silicon was successfully achieved, leading to the formation of a high-quality vertical Schottky junction that exhibited excellent optoelectronic performance. The photodetector fabricated based on this Schottky junction demonstrated a broadband responsivity ranging from 390 to 1025 nm, demonstrating commendable sensitivity across this broad spectrum of wavelengths. While conventional detectors made of 2D materials/silicon junction typically sensitive up to wavelengths ≈900 nm, our fabricated photodetector exhibited remarkable sensitivity, delivering a satisfactory performance even at extended wavelengths up to 1025. Notably, this detector surpassed other counterparts based on various 2D materials and silicon in terms of sensitivity. Additionally, the very fast response time of this detector, with rise and fall times of 35 and 225 μs, respectively, outperformed traditional 2D material detectors significantly. Simulation results validated the optoelectronic behavior observed experimentally at this electrical junction, hinting those further enhancements to this structure could yield even speedier response times. This study illustrates that employing the direct growth technique of borophene on selected substrates using the Al-activated CVD method could pave the way for researchers in high-performance borophene-based electronic device fabrication.

4. Experimental Section

Device Fabrication: The fabrication process, illustrated schematically in Figure S3 (Supporting Information), starts by cleaning an n-type (100) silicon wafer using RCA-1 solution. This solution consists of deionized water, oxygenated water, and ammonia in a 5:1:1 ratio. Following the cleaning step, a 200 nm silicon dioxide (SiO_2) was deposited onto the silicon wafer through a thermal oxidation process at 1100 °C. Then, a 20-nm aluminum layer was deposited using physical vapor deposition (PVD) with a base pressure of 3×10^{-6} torr. Standard photolithography technique was then employed to create square patterns with a width of 50 μm on the deposited layers. These squares define the regions for selective etching, where both the aluminum and SiO_2 layers were removed. The active area of the detector includes numerous squares within a 2×2 mm^2 region. The optical image depicted in Figure 1b exhibits one of these etched areas.

Subsequently, the patterned sample was placed inside a CVD chamber. The chamber was evacuated to a pressure of 2×10^{-3} torr, and the temperature was raised to 600 °C over 15 min. During a 10-min annealing step in the presence of H_2, aluminum begins to aggregate (as seen in the optical image of Figure 1b). A continuous flow of hydrogen gas (20 SCCM) was maintained throughout this stage. Following this, the hydrogen flow rate was increased to 40 SCCM, and diborane (B_2H_6) was introduced into the chamber with the flow rate of 15 SCCM. Diborane was produced from sodium borohydride and sulfuric acid according to the proposed technique of reference.[15]

The role of aluminum was crucial for borophene growth. Boron atoms in borophene exhibit electron deficiency, necessitating the presence of a metallic layer (such as aluminum) to supply electrons. Upon introducing B_2H_6, borophene growth initiates in regions where aluminum islands have formed on the silicon dioxide. As the growth process continues, borophene layers become larger, pushing back the aluminum islands and extending toward the silicon region. Finally, the diborane flow was terminated, and the chamber gradually cools to room temperature over 3 h. The borophene layers continue to grow on the silicon, now free from aluminum. AFM images (Figure 1c–e) show the evolution of borophene growth from lithographically defined edge regions toward the silicon area. After the growth, gold and Al layers were deposited as top and bottom

 © 2024 The Author(s). Advanced Materials Interfaces published by Wiley-VCH GmbH

21967350, 2025, 8, Downloaded from https://advanced.onlinelibrary.wiley.com/doi/10.1002/admi.202400894 by Christian-Albrechts-Universitat zu Kiel, Wiley Online Library on [16/10/2025]. See the Terms and Conditions (https://onlinelibrary.wiley.com/terms-and-conditions) on Wiley Online Library for rules of use; OA articles are governed by the applicable Creative Commons License

contacts using PVD system. As shown in Figure 1f,g, at the end of the growth step, the active area of the detector was almost covered by borophene.

Structural and Morphological Characterizations: Field-emission scanning electron microscope (FESEM-4160, Hitachi, Japan) and an AFM (NT-MDT) were used for morphological analyses. Lattice images and electron diffraction patterns to study the atomic structure of the synthesized borophene were acquired by HRTEM (Hitachi 4160) at accelerating voltage of 80 kV. For HRTEM characterizations, 2D borophene sheets were transferred onto carbon-coated Cu grids using the transferring method reported in reference.[15] Structural analyses were also investigated by Raman spectroscopy (Raman Takram P50C0R10). A continuous-wave green solid-state laser at the power of 20 mW, carefully filtered, served as the Raman excitation source (wavelength $\lambda = 532$ nm).

Optoelectronic Characterization: Optoelectronic characterizations were performed at room temperature using a source unit IVM-2.10.15 (Nano Pajouhan Raga Co., Iran). The acquisition time for measuring photocurrent was set to 100 ms, and averaging was performed over 100 data points to increase the signal-to-noise ratio. Light emitting diodes with different peak intensities from 360 to 1025 nm were used as light sources.

CL Measurements: CL measurements were performed using CL detector (DELMIC SPARC system) and optical analyzers integrated with a Zeiss-SIGMA field-emission SEM. As shown schematically in Figure 5a, the generated photons from the interaction between the electron beam and borophene sheets were gathered using a parabolic mirror and then directed toward the CL detector. To an optimal photon collection, the sample was carefully positioned at the focal point of the mirror. For CL spectral mapping, the electron beam spot size, acquisition time, and beam current were set to be 20 nm, 200 ms, and 9nA, respectively. The collected data were analyzed using ODEMIS, a Python-based freeware. The data were then exported as CSV files and imported into MATLAB for further analysis and visualization.

DFT Calculations: In this study, DFT calculations was conducted using Quantum ESPRESSO. The electron–ion interactions were modeled with optimized norm-conserving Vanderbilt pseudopotentials. For the exchange and correlation energies, the generalized gradient approximation was utilized following the Perdew–Burke–Ernzerhof method. All calculations were performed with a plane wave cut-off energy of 50 Hartree. The relaxation process employed an $8 \times 8 \times 1$ k-point mesh and a force threshold of 10^{-5}. To calculate the dielectric tensor, these steps were followed: initially, a self-consistent field (SCF) calculation was performed using an $8 \times 8 \times 1$ k-point mesh and 16 bands. Next, the calculation was refined with a $32 \times 32 \times 1$ k-point mesh and 1000 bands for the non-self-consistent field (NSCF) calculation. Finally, a post-processing step was carried out to obtain the dielectric tensor.

FDTD Simulations: The computational model employed in this study utilizes the FDTD method. Through simulations, the optical absorption and carrier generation rates of the device across the spectrum ranging from 310 to 1250 nm were investigated. Subsequently, the carrier generation rate data for electrical simulations were utilized. The unit cell of the structure was assumed to have periodic boundary conditions in the $\pm x$ directions, while perfectly matched layers were implemented along the y direction. The size of the unit cell is $5 \times 150\ \mu m^2$. The borophene sheet was considered to be uniform and a monolayer. For precise results and numerical convergence, a fine mesh was applied with $d_y = 0.1$ nm (in the y-direction) and $d_x = 0.2$ µm (in the x-direction) for borophene, and $d_y = 0.2$ µm and $d_x = 0.2$ µm for silicon. The optical source, which illuminates the top surface of the device, emits a monochromatic optical plane wave with a fixed intensity at each wavelength.

In FDTD simulations, the permittivity tensor at each frequency of ω, obtained from DFT, was diagonalized for simplifying computations as follows

$$\epsilon_D = U\epsilon U^{\dagger} \tag{7}$$

where U is a unitary matrix, $U\dagger$ is the complex conjugate transpose of U, and ϵ_D is the diagonalized permittivity matrix. The grid attribute in FDTD was used to apply the material's transformation matrix to the simulation grid. When working with anisotropic materials, the grid attribute ensures that the electric field components were aligned with the principal axes of the diagonalized permittivity tensor. This alignment allows the simulation to correctly model the anisotropic behavior of the material. To that end, the diagonal values of ϵ_D were entered into the materials database, after which a matrix transformation grid attribute was added using the calculated U matrix.

In the next step, the absorption power was calculated in every wavelength to produce the carrier generation rate data utilized for further electrical simulations. Finally, the carrier generation rate was obtained by integrating the generation rate over the simulation spectrum. These generation rates calculated for each angular frequency to obtain electrical properties such as the current–voltage plots of the simulated system under dark and illuminated conditions.

Supporting Information

Supporting Information is available from the Wiley Online Library or from the author.

Acknowledgements

This project has received funding from the European Research Council (ERC) under the European Union's Horizon 2020 research and innovation programme under grant agreement no. 802130 (Kiel, NanoBeam), from the Deutsche Forschungsgemeinschaft under Grant agreement nos. 525347396 and 447330010, and from the Volkswagenstiftung (Momentum Grant).

Conflict of Interest

The authors declare no conflict of interest.

Author Contributions

The manuscript was prepared through contributions of all authors. All authors provided their approval to the final version of the manuscript.

Data Availability Statement

The data that support the findings of this study are available from the corresponding author upon reasonable request.

Keywords

2D materials, borophene, chemical vapor deposition, photodetectors, Schottky, silicon

Received: November 11, 2024
Revised: December 17, 2024
Published online: December 25, 2024

[1] T. H. Han, H. Kim, S. J. Kwon, T. W. Lee, *Materials Science and Engineering R: Reports.* **2017**, *118*, 1.
[2] A. Hekmatikia, Y. Abdi, *IEEE Electron Device Lett.* **2018**, *39*, 216.
[3] S. Darbari, V. Ahmadi, P. Afzali, Y. Abdi, M. Feda, *J. Nanopart. Res.* **2014**, *16*, 2798.

© 2024 The Author(s). Advanced Materials Interfaces published by Wiley-VCH GmbH

[4] A. Hayat, T. Bashir, A. M. Ahmed, Z. Ajmal, M. M. Alghamdi, A. A. El-Zahhar, M. Sohail, M. A. Amin, Y. Al-Hadeethi, E. Ghasali, S. Raza, Y. Orooji, *Materials Science and Engineering: R: Reports.* **2024**, *159*, 100796.
[5] F. Larki, Y. Abdi, P. Kameli, H. Salamati, *Photonic Sensors.* **2022**, *12*, 31.
[6] X. Liu, G. Wu, J. Zeng, C. Bai, W. Li, J. Wang, J. Chu, *Appl. Phys. Lett.* **2023**, *122*, 193101.
[7] X. Chen, H. Chen, Y. Sun, S. Zhang, Y. Xia, D. W. Zhang, P. Zhou, W. Li, Z. Sun, W. Bao, *2D Mater.* **2022**, *9*, 035015.
[8] Y. Yi, X.-F. Yu, W. Zhou, J. Wang, P. K. Chu, *Materials Science and Engineering: R: Reports.* **2017**, *120*, 1.
[9] Z. Xie, T. Zhao, X. Yu, J. Wang, *Small.* **2024**, *20*, 2311621.
[10] Z. Dehghani, M. Nadafan, M. B. Mohammadzadeh Shamloo, Z. Shadrokh, S. Gholipour, M. H. R. Manshadi, S. Darbari, Y. Abdi, *Opt. Laser Technol.* **2022**, *155*, 108352.
[11] F. Xia, T. Mueller, Y. Lin, A. Valdes-Garcia, P. Avouris, *Nat. Nanotechnol.* **2009**, *4*, 839.
[12] M. Mathew, C. S. Rout, *J Mater Chem C Mater.* **2021**, *9*, 395.
[13] H. S. Naghavi, M. B. M. Shamloo, S. Darbari, Y. Abdi, *IEEE Sens. J.* **2023**, *23*, 30311.
[14] M. Javadi, A. Noroozi, A. Mazaheri, Y. Abdi, *Adv. Opt. Mater.* **2019**, *7*, 1900470.
[15] A. Mazaheri, M. Javadi, Y. Abdi, *ACS Appl. Mater. Interfaces.* **2021**, *13*, 8844.
[16] Y. Abdi, A. Mazaheri, S. Hajibaba, S. Darbari, S. J. Rezvani, A. Di Cicco, F. Paparoni, R. Rahighi, S. Gholipour, A. Rashidi, M. M. Byranvand, M. Saliba, *ACS Mater. Lett.* **2022**, *4*, 1929.
[17] Y. Liu, G. Tai, C. Hou, Z. Wu, X. Liang, *ACS Appl. Mater. Interfaces.* **2023**, *15*, 14566.
[18] Z. Wu, G. Tai, R. Liu, C. Hou, W. Shao, X. Liang, Z. Wu, *ACS Appl. Mater. Interfaces.* **2021**, *13*, 31808.
[19] S. M. Hosseini, A. Imanpour, M. Rezavand, A. M. A. Tash, S. Antonini, S. J. Rezvani, Y. Abdi, *ACS Mater. Lett.* **2024**, *6*, 933.
[20] J. Nong, F. Feng, J. Gan, C. Min, X. Yuan, M. Somekh, *Adv. Opt. Mater.* **2022**, *10*, 2102131.
[21] B. Feng, J. Zhang, Q. Zhong, W. Li, S. Li, H. Li, P. Cheng, S. Meng, L. Chen, K. Wu, *Nat. Chem.* **2016**, *8*, 563.
[22] A. J. Mannix, X.-F. Zhou, B. Kiraly, J. D. Wood, D. Alducin, B. D. Myers, X. Liu, B. L. Fisher, U. Santiago, J. R. Guest, M. J. Yacaman, A. Ponce, A. R. Oganov, M. C. Hersam, N. P. Guisinger, *Science.* **2015**, *350*, 1513.
[23] A. Rahman, M. T. Rahman, M. A. Chowdhury, S. Bin Ekram, M. M. K. Uddin, M. d. R. Islam, L. Dong, *Sens Actuators A Phys.* **2023**, *359*, 114468.
[24] B. Feng, J. Zhang, R.-Y. Liu, T. Iimori, C. Lian, H. Li, L. Chen, K. Wu, S. Meng, F. Komori, I. Matsuda, *Phys. Rev. B.* **2016**, *94*, 041408.
[25] H. Xiao, W. Cao, T. Ouyang, S. Guo, C. He, J. Zhong, *Sci. Rep.* **2017**, *7*, 45986.
[26] E. S. Penev, A. Kutana, B. I. Yakobson, *Nano Lett.* **2016**, *16*, 2522.
[27] Z. Zhang, Y. Yang, E. S. Penev, B. I. Yakobson, *Adv. Funct. Mater.* **2017**, *27*, 1605059.
[28] Z. Wu, X. Liang, Y. Liu, M. Xu, R. Zhu, G. Tai, *Angew. Chem., Int. Ed.* **2024**, 202416041.
[29] Z. Wu, X. Liang, Z. Zhao, Q. Wu, X. Liu, Y. Liu, M. Xu, C. Hou, G. Tai, *Chem. Eng. J.* **2024**, *500*, 156881.
[30] Y. Abdi, M. Taleb, S. Hajibaba, M. Moayedi, N. Taleb, arXiv:2404.13609
[31] S. J. Rezvani, Y. Abdi, R. Parmar, F. Paparoni, S. Antonini, R. Gunnella, A. Di Cicco, M. Amati, L. Gregoratti, A. Mazaheri, S. Hajibaba, *ACS Appl. Nano Mater.* **2024**, *7*, 13712.
[32] S. Sheng, J.-B. Wu, X. Cong, Q. Zhong, W. Li, W. Hu, J. Gou, P. Cheng, P.-H. Tan, L. Chen, K. Wu, *ACS Nano.* **2019**, *13*, 4133.
[33] G. Shao, *Environmental Materials.* **2021**, *4*, 273.
[34] A. Di Bartolomeo, G. Luongo, L. Iemmo, F. Urban, F. Giubileo, *IEEE Trans. Nanotechnol.* **2018**, *17*, 1133.
[35] A. Alù, M. G. Silveirinha, A. Salandrino, N. Engheta, *Phys. Rev. B.* **2007**, *75*, 155410.
[36] V. Caligiuri, M. Palei, M. Imran, L. Manna, R. Krahne, *ACS Photonics.* **2018**, *5*, 2287.
[37] S. A. Maier, *Plasmonics: Fundamentals and Applications*, Springer US, New York **2007**.
[38] D. Ma, R. Wang, J. Zhao, Q. Chen, L. Wu, D. Li, L. Su, X. Jiang, Z. Luo, Y. Ge, J. Li, Y. Zhang, H. Zhang, *Nanoscale.* **2020**, *12*, 5313.
[39] G. Tai, B. Liu, C. Hou, Z. Wu, X. Liang, *Nanotechnology.* **2021**, *32*, 505606.
[40] X. Liang, C. Hou, Z. Wu, Z. Wu, G. Tai, *Nanotechnology.* **2023**, *34*, 5826.
[41] M. Taleb, F. Davoodi, F. K. Diekmann, K. Rossnagel, N. Talebi, *Adv. Photonics Res.* **2022**, *3*, 2100124.
[42] M. Taleb, M. Hentschel, K. Rossnagel, H. Giessen, N. Talebi, *Nat. Phys.* **2023**, *19*, 869.
[43] T. Coenen, N. M. Haegel, *Appl. Phys. Rev.* **2017**, *4*, 031103.
[44] B. J. M. Brenny, T. Coenen, A. Polman, *J. Appl. Phys.* **2014**, *115*,.
[45] M. J. Pinheiro, *Appl. Sci.* **2024**, *14*, 1833.
[46] J.-X. Sun, H.-C. Yang, Y. Li, H.-J. Cui, *Phys. Rev. Appl.* **2023**, *20*, 034061.
[47] P. Caprioglio, M. Stolterfoht, C. M. Wolff, T. Unold, B. Rech, S. Albrecht, D. Neher, *Adv. Energy Mater.* **2019**, *9*.
[48] L. Q. Phuong, S. M. Hosseini, O. J. Sandberg, Y. Zou, H. Y. Woo, D. Neher, S. Shoaee, *Sol. RRL.* **2021**, *5*, 2000649.

© 2024 The Author(s). Advanced Materials Interfaces published by Wiley-VCH GmbH

21967350, 2025, 8, Downloaded from https://advanced.onlinelibrary.wiley.com/doi/10.1002/admi.202400894 by Christian-Albrechts-Universitat zu Kiel, Wiley Online Library on [16/10/2025]. See the Terms and Conditions (https://onlinelibrary.wiley.com/terms-and-conditions) on Wiley Online Library for rules of use; OA articles are governed by the applicable Creative Commons License